

Dynamics and Pinning for Skyrmions in Altermagnets

J. C. Bellizotti Souza,^{1,*} C. J. O. Reichhardt,² A. Saxena,² and C. Reichhardt²

¹“Gleb Wataghin” Institute of Physics, University of Campinas, 13083-859 Campinas, São Paulo, Brazil

²Theoretical Division and Center for Nonlinear Studies,

Los Alamos National Laboratory, Los Alamos, New Mexico 87545, USA

(Dated: February 24, 2026)

We examine the dynamics, Hall angle, and pinning for Néel skyrmions in an altermagnet. Using an atomistic model, we show that skyrmion velocity and Hall angle dependence is anisotropic with respect to the direction of the drive, due to the fourfold symmetry implied by the two sublattices of the altermagnet. The skyrmion Hall angle and velocity at fixed drive show strong variations for increasing ratios of the exchange constant of the sublattices, J_2/J_1 . This fourfold anisotropy of altermagnetic (ATM) skyrmions also leads to anisotropic pinning effects for an ATM skyrmion interacting with isotropic circular pinning sites. We also propose a simple particle model for this system that takes into account this anisotropy and find that it captures both the variations of the ATM skyrmion Hall angle and velocity as a function of drive direction, as also found in the atomistic simulations. Using this particle model, we examine ATM skyrmions interacting with a periodic array of pinning sites. For increasing ratios of J_2/J_1 , we find a strongly non-monotonic ATM skyrmion velocity, where there is a minimum in the velocity where the skyrmion locks to different symmetry directions of the periodic pinning lattice. For a random array, we find that ATM skyrmions show strongly anisotropic depinning thresholds and velocity responses for different drive directions, and that the Hall angle is nearly constant with drive. In comparison, for the same parameters, the depinning threshold for a ferromagnetic (FM) skyrmion is lower, and the skyrmion Hall angle shows a strong velocity dependence. The lower depinning threshold for FM skyrmions is due to stronger Magnus forces.

I. INTRODUCTION

Skyrmions are topological magnetic textures that typically arise in chiral magnets and were first observed in neutron scattering experiments¹ and soon after with direct imaging^{2,3}. Since then, the field has undergone rapid growth as more systems have been found that can support skyrmions^{4–11}. Skyrmions can be moved with an applied current and via various other methods. They experience a pinning effect upon interacting with quenched disorder¹², so there is typically a current or depinning threshold for skyrmion motion^{6,13–16}. Skyrmions can be characterized by a winding number Q . Due to their topology, they can have a strong Magnus or gyroscopic component to their motion^{8,14,17–21}, which causes skyrmions to move at an angle with respect to the applied drive, known as the skyrmion Hall angle. The Magnus effect also influences how skyrmions interact with quenched disorder, which can lead to spiral-like motion of skyrmions around pinning sites. Due to their size, stability, and mobility, skyrmions are also promising candidates for a number of applications, such as racetrack memory^{22,23} and novel skyrmion-based computing^{24,25}.

There are also different types of skyrmions and related magnetic textures that include antiskyrmions^{26,27}, merons²⁸ antiferromagnetic skyrmions^{29–31}, skyrmionium³², and three-dimensional (3D) Hopfions^{33–35}. These textures can exhibit distinct dynamics, lattice structures, and interactions with pinning^{35,36}. For applications, the large skyrmion Hall angle presents a barrier for creating certain devices. For example, when skyrmions move along a racetrack, the finite Hall angle causes them to move to the sample edge where they can annihilate. There have been various efforts to find materials to reduce the skyrmion Hall effect, such as by using skyrmionium with a topological charge of $Q = 0$; however, skyrmion-

ium is unstable at higher drives or strong pinning and breaks up into skyrmions with $Q = 1$ ^{32,37}. One of the most promising systems in which the skyrmion Hall effect is absent or small is antiferromagnetic skyrmions^{29,30,38,39}, which can be regarded as two coupled ferromagnetic skyrmions in which the net topological charge cancels. Various experiments have been able to realize such textures³⁰ and show that fast motion under a drive with small skyrmion Hall angles can occur^{31,40}. In general, there has been growing interest in antiferromagnets for both basic science and technological applications⁴¹.

Recently, a new type of magnet called an altermagnet has been proposed^{42–46}, which has zero macroscopic magnetization but can exhibit finite higher-order magnetic moments that break Kramers degeneracy. A candidate material is MnTe⁴⁷. This class of systems has similarities to antiferromagnets, but the symmetry transitions are different, since altermagnets can be considered as consisting of two partially overlapping sublattices. Several experiments have found evidence for altermagnetism^{48,49}. A natural question is whether altermagnet systems can also host skyrmions and, if so, how such skyrmions would behave under driving and interaction with pinning. There have already been several investigations of altermagnet (ATM) skyrmions^{50–54}. Jin *et al.*⁵⁰ found that ATM skyrmions can have a finite skyrmion Hall angle due to the formation of an effective quadrupole interaction, and that this Hall angle can depend on the direction of the applied drive. Jin *et al.* also proposed a Thiele-like equation of motion for ATM skyrmions, which they verified with micromagnetic simulations. Vakili *et al.*⁵¹ found that skyrmions in altermagnet systems can exhibit an anisotropic skyrmion Hall effect, while Schwartz *et al.*⁵² found that ATM skyrmions could be moved with a thermal gradient. Jiang *et al.*⁵³ studied the quadrupolar nature of ATM skyrmions and argued that they could be used as an ideal system to explore systems with d -wave symmetry.

Liu *et al.*⁵⁴ considered current driving in skyrmions in frustrated altermagnet systems and found that the skyrmion Hall angle does not lock to the skyrmion helicity. Overall, these studies have provided insights into the unique properties and behaviors of skyrmions in altermagnet systems, which could have important implications for potential applications.

In this work, we consider atomistic simulations of the dynamics and pinning of ATM skyrmions. We find that the ATM skyrmion velocity and Hall angle are strongly dependent on the direction of the driving force, due to the anisotropic nature of the quadrupole moment that arises from the two ATM sublattices with exchange constants J_1 and J_2 . For different drive directions, we show how the velocity varies with increasing J_2/J_1 , where a larger J_2/J_1 ratio leads to smaller and more anisotropic skyrmions. As J_2/J_1 increases, the skyrmion velocity and Hall angle exhibit an anisotropic response. For ATM skyrmions interacting with isotropic circular pinning sites, we find that the pinning site energy and depinning force are anisotropic. We also propose a particle-based model of ATM skyrmions, which is simpler than the model of Jin *et al.*⁵⁰ in that it does not take into account skyrmion distortions, but instead assumes different dissipation components along each axis. This particle model shows strong agreement with the anisotropic velocity and Hall angle response found from the atomistic simulations. Using this model, we examine the interaction of an ATM skyrmion with a pinning array and find that the pinning efficiency is enhanced at certain values of J_2/J_1 , where the skyrmion Hall angle is large enough that the skyrmion motion can lock to the different symmetry directions of the pinning lattice. For ATM skyrmion interactions with random pinning for different drive directions, we find that the depinning threshold and skyrmion sliding velocity are strongly anisotropic, and that the pinning strength is stronger than what is observed for ferromagnetic skyrmions. We argue that this is due to the lower Magnus force in the ATM system, which causes the gyroscopic motion of the ATM skyrmions to be too weak to permit the skyrmions to slide around the pinning sites. Finally, we discuss some future directions for the study of ATM skyrmion systems.

II. SIMULATION

We consider a two sublattice model, capable of hosting Néel ATM skyrmions, governed by the following Hamiltonian⁵⁰

$$\begin{aligned} \mathcal{H} = & - \sum_i J_1 (\mathbf{m}_i^A \cdot \mathbf{m}_{i+\hat{x}}^A + \mathbf{m}_i^B \cdot \mathbf{m}_{i+\hat{y}}^B) \\ & - \sum_i J_2 (\mathbf{m}_i^A \cdot \mathbf{m}_{i+\hat{y}}^A + \mathbf{m}_i^B \cdot \mathbf{m}_{i+\hat{x}}^B) \\ & - \sum_i J_3 \mathbf{m}_i^A \cdot \mathbf{m}_i^B \\ & - \sum_{i,\langle i,j \rangle} \mathbf{D}_{i,j} \cdot (\mathbf{m}_i^A \times \mathbf{m}_j^A + \mathbf{m}_i^B \times \mathbf{m}_j^B) \\ & - \sum_i K \left[(\hat{z} \cdot \mathbf{m}_i^A)^2 + (\hat{z} \cdot \mathbf{m}_i^B)^2 \right]. \end{aligned} \quad (1)$$

Here J_1 is the first exchange constant, present along x bonds on sublattice A and along y bonds on sublattice B . J_2 is the second exchange constant, present along y bonds on sublattice A and along x bonds on sublattice B . J_3 is an antiferromagnetic ($J_3 < 0$) coupling between sublattices A and B . Schematics showing the geometry of the exchange interactions appear in Fig. 1(b, c, d). The next interaction is the interfacial Dzyaloshinskii-Moriya (DM) interaction, where $\mathbf{D}_{i,j} = D\hat{z} \times \hat{\mathbf{r}}_{i,j}$ is the DM vector and $\hat{\mathbf{r}}_{i,j}$ is the unit distance vector between sites i and j . This interaction is present only between two sites of the same sublattice. Here $\langle i, j \rangle$ indicates that the sum is performed over the first neighbors of the i th-site. The last interaction is the perpendicular magnetic anisotropy (PMA) with constant K . As shown in Fig. 1(b, c, d), the underlying lattice is a square arrangement of atoms with lattice constant a .

The time evolution is obtained by means of the Landau-Lifshitz-Gilbert equation augmented with external torque contributions⁵⁵⁻⁵⁷,

$$\frac{\partial \mathbf{m}_i^l}{\partial t} = -\gamma \mathbf{m}_i^l \times \mathbf{H}_{i,l}^{\text{eff}} + \alpha \mathbf{m}_i^l \times \frac{\partial \mathbf{m}_i^l}{\partial t} + \boldsymbol{\tau}_i^l. \quad (2)$$

Here $\gamma = 1.76 \times 10^{11} \text{ T}^{-1} \text{ s}^{-1}$ is the electron gyromagnetic ratio, $\mu = \hbar\gamma$ is the atomic magnetic moment, $l = A, B$ is the sublattice, $\mathbf{H}_{i,l}^{\text{eff}} = -\frac{1}{\mu} \frac{\partial \mathcal{H}}{\partial \mathbf{m}_i^l}$ is the effective magnetic field including all interactions from the Hamiltonian, α is the phenomenological damping introduced by Gilbert, and the last term is the spin-transfer-torque (STT) contribution caused by application of an in plane spin polarized current. We consider interactions between conduction electrons and our sample in the exchange-dominant regime, so that STT contributions are given by

$$\boldsymbol{\tau}_i^l = \frac{\hbar\gamma p a^3}{2e\mu} \left[(\nabla \cdot \mathbf{j}) \mathbf{m}_i^l - \beta \mathbf{m}_i^l \times (\nabla \cdot \mathbf{j}) \mathbf{m}_i^l \right], \quad (3)$$

where p is the spin polarization, e the electron charge, and $\mathbf{j} = j(\cos\phi\hat{x} + \sin\phi\hat{y})$ the applied current density. The first term is the adiabatic contribution, and the second term the non-adiabatic contribution, with β the non-adiabatic coefficient. We emphasize that ∇ only acts on a given sublattice l ; this also can be seen by $\mathbf{j} \cdot \hat{z} = 0$. Use of this STT expression implies that the conduction electron spins are always parallel to the magnetic moments $\mathbf{m}^{6,58}$, or equivalently, that we are considering interactions between conduction electrons and our sample to be in the exchange-dominant regime⁵⁰.

In this work we fix $J_1 = 1 \text{ meV}$, $J_3 = -0.05J_1$, $D = 0.2J_1$, $K = 0.04J_1$, $a = 0.5 \text{ nm}$, and $\beta = 0.005$. The numerical integration of Eq. 2 is performed using a fourth order Runge-Kutta method, with an integration step of $\Delta t = 0.01\hbar/J_1 \approx 0.6 \text{ ps}$.

III. RESULTS

In Fig. 2(a) we plot the skyrmion Hall angle θ_{Hall} versus drive angle ϕ for a system with $J_2/J_1 = 3$ at different values of the driving current j , computed using the two sublattice

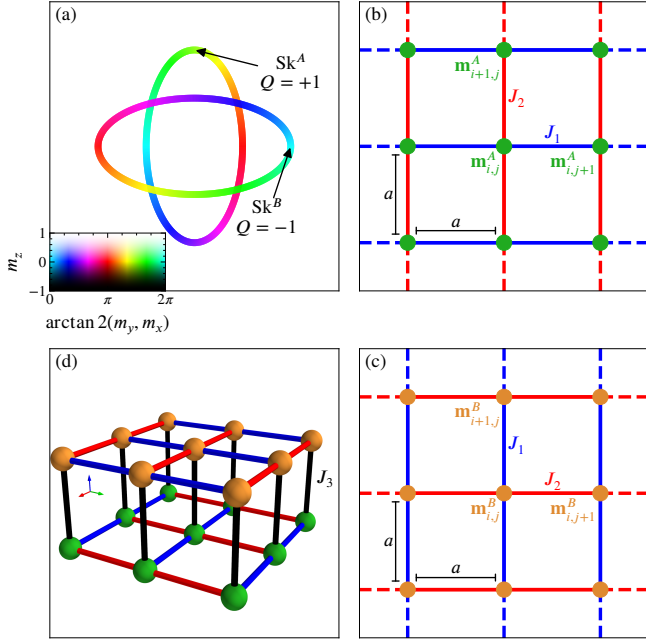


FIG. 1. (a) Schematic showing ATM skyrmions on sublattices A and B . Sublattice A (B) skyrmions have $Q = +1$ ($Q = -1$), so the sample has no net topological charge. Inset: colormap used to represent skyrmions throughout this work. The colors in the main panel correspond to $m_z = 0$. As a consequence of the anisotropic exchange interactions, the skyrmions become elliptical. (b) Schematic of sublattice A showing the square arrangement of atoms with lattice constant a and the magnetic moment $\mathbf{m}_{i,j}^A$ (green). Bonds along y have exchange constant J_2 (red) and bonds along x have exchange constant J_1 (blue), giving an anisotropic exchange interaction. (c) The corresponding schematic of sublattice B with magnetic moments $\mathbf{m}_{i,j}^B$ (orange). The exchange constants are swapped: bonds along y have exchange constant J_1 (blue) and bonds along x have exchange constant J_2 (red). (d) Three-dimensional view of a portion of our sample showing sublattices A (green) and B (orange) along with exchange constants J_1 (blue) and J_2 (red). A third exchange constant J_3 (black) couples sublattices A and B along z .

model described in Eq. (1). Here the ATM skyrmion Hall angle passes through zero at $\phi = \pi/4 + n\pi/2$ with $n \in \mathbb{Z}$. The ATM skyrmion is expected to have 45° symmetry, implying that currents applied along the directions of the ATM skyrmion nodes should have an equivalent effect on the overall texture; however, this is not what we observe. Instead of the sinusoidal curve found in Jin *et al.*⁵⁰, Fig. 2(a) shows that there is a sawtooth dependence of θ_{Hall} on ϕ . We extract the maximum Hall angle value $\theta_{\text{Hall}}^{\text{max}}$ from each of the curves in Fig. 2(a) and plot it as a function of j in Fig. 2(b), where we find that the data are fit well by an exponential curve. As for the net velocity $v = \sqrt{v_x^2 + v_y^2}$ of the ATM skyrmion, the plot of v versus ϕ in Fig. 2(c) at different currents j shows that v has an oscillatory behavior, with peak velocities appearing at $\phi = 3\pi/4 + n\pi$ and local velocity minima at $\phi = \pi/4 + n\pi$ with $n \in \mathbb{Z}$. This behavior is the opposite of what is found for regular ferromagnetic skyrmions, where the skyrmion velocity is independent of the direction in which the current is ap-

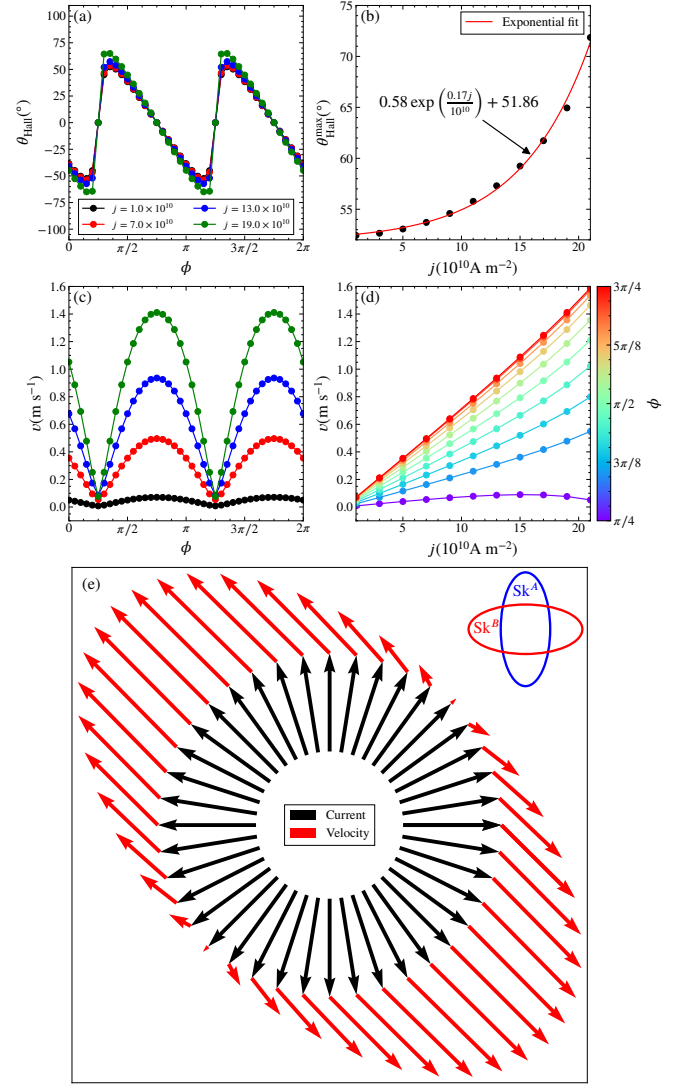


FIG. 2. Simulation results for an ATM system with $J_2/J_1 = 3$. (a) The skyrmion Hall angle θ_{Hall} vs current direction ϕ at $j = 1.0 \times 10^{10}$ (black), 7.0×10^{10} (red), 13.0×10^{10} (blue), and 19.0×10^{10} (green). (b) The maximum Hall angle $\theta_{\text{Hall}}^{\text{max}}$ across all ϕ values vs j (black) along with an exponential fit (red). (c) ATM skyrmion velocity, $v = \sqrt{v_x^2 + v_y^2}$, vs ϕ at the same j values from panel (a). (d) v vs j at different values of ϕ . (e) Schematic of the current direction (black arrows) and the corresponding ATM skyrmion velocity (red arrows). Red arrows are in scale with respect to one another. The inset shows the two skyrmions on each sublattice, with nodes occurring where the curves cross.

plied. We plot v versus j for different values of ϕ in Fig. 2(d). Here, at $\phi = \pi/4$, v is close to zero. As ϕ increases, the dependence of v on j becomes more linear, until for the peak velocity values at $\phi = 3\pi/4$, v varies completely linearly with j . To understand this behavior, in Fig. 2(e) we plot a schematic of the dependence of the ATM skyrmion velocity on the direction of the applied current. Here we see that ATM skyrmions only move along $3\pi/4$ or $-\pi/4$, with the motion angle changing sign at drives aligned with $\phi = \pi/4$ and $\phi = -3\pi/4$. The

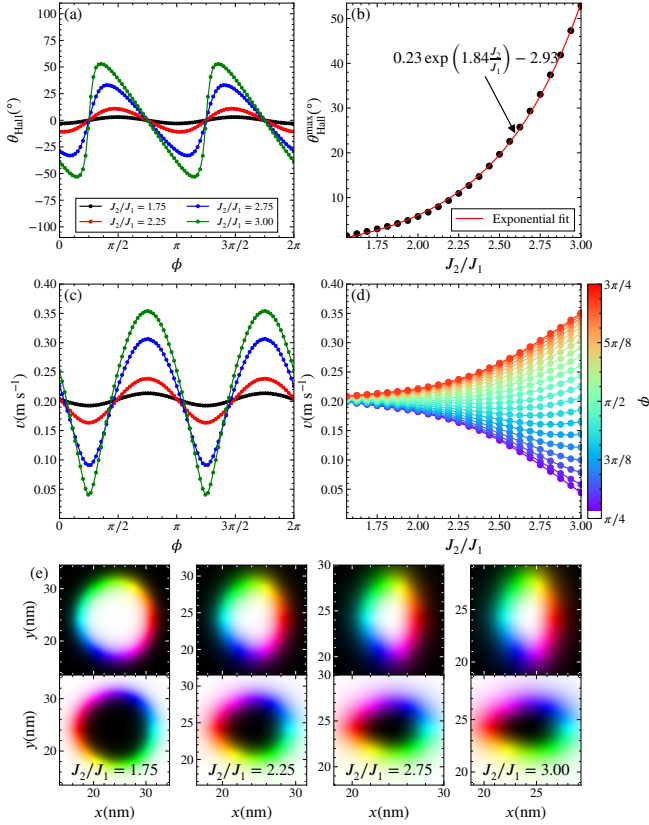


FIG. 3. Simulation results for an ATM system with $j = 5 \times 10^{10} \text{ A m}^{-2}$. (a) θ_{Hall} vs ϕ at $J_2/J_1=1.75$ (black), 2.25 (red), 2.75 (blue), and 3.00 (green). (b) The maximum Hall angle $\theta_{\text{Hall}}^{\text{max}}$ across all ϕ values vs J_2/J_1 (black) along with an exponential fit (red). (c) Skyrmion velocity v vs ϕ at the J_2/J_1 values from (a). (d) v vs J_2/J_1 for different ϕ values. (e) Real space images of different ATM skyrmion configurations in the two layers with different J_2/J_1 .

inset of Fig. 2(e) indicates that the angles at which the motion angle changes sign match the directions of the ATM skyrmion nodes. The peak and minimum velocity values in Fig. 2(c) also fall along the node directions.

Figure 3(a) shows θ_{Hall} versus ϕ at a fixed current of $j = 5 \times 10^{10} \text{ A m}^{-2}$ for different J_1/J_2 ratios. We find that θ_{Hall} has a sawtooth shape at higher J_2/J_1 , but as J_2/J_1 decreases, the amplitude of the variations in θ_{Hall} decreases and the curve becomes more sinusoidal in shape. In the $J_2/J_1 = 1$ limit, θ_{Hall} approaches a constant value of $\theta_{\text{Hall}} = 0$. The skyrmions at $J_2/J_1 = 1$ are symmetrical and have zero net topological charge, corresponding to an antiferromagnetic skyrmion. We find that for all J_2/J_1 ratios, θ_{Hall} passes through zero when $\phi = \pi/4 + n\pi/2$, with $n \in \mathbb{Z}$. The plot of the maximum Hall value $\theta_{\text{Hall}}^{\text{max}}$ versus J_2/J_1 in Fig. 3(b) also has an exponential shape. Comparing Fig. 3(b) with Fig. 2(b), we observe a stronger dependence of $\theta_{\text{Hall}}^{\text{max}}$ on J_2/J_1 than with j , as indicated by the exponential factors of both fits. Figure 3(c) shows the skyrmion velocity v versus ϕ at different values of J_2/J_1 . At higher J_2/J_1 , v resembles a rectified sinusoidal curve, while at lower J_2/J_1 , v is closer to a pure sinusoidal shape. The amplitude of the velocity variations as a function

of ϕ is a strong function of J_2/J_1 . In the $J_2/J_1 = 1$ limit, v approaches a constant value of $v \approx 20 \text{ m s}^{-1}$. The behavior at lower J_2/J_1 is in accordance with the observations in Ref. 50. We find velocity minimums at $\phi = \pi/4 + n\pi$, with $n \in \mathbb{Z}$, and velocity peaks at $\phi = 3\pi/4 + n\pi$, with $n \in \mathbb{Z}$. The minimum velocity values approach $v = 0$ as J_2/J_1 increases. We show v versus J_2/J_1 for a range of different ϕ values in Fig. 3(d). The peak ATM skyrmion velocity increases rapidly with increasing J_2/J_1 , while the minimum velocity rapidly decreases towards $v = 0$ as J_2/J_1 becomes larger. Real space images of the ATM skyrmion configurations at different values of J_2/J_1 appear in Fig. 3(e). The ATM skyrmions are smaller and more asymmetrical at higher J_2/J_1 , and become larger and more symmetrical for lower J_2/J_1 .

Jin *et al.*⁵⁰ constructed a quantitatively accurate model for ATM skyrmions that correctly predicts the behavior of ATM skyrmions, with results matching those of simulations; however, below we show that this is not the simplest model capable of explaining the asymmetric ATM skyrmion behavior. Instead, we claim that the simplest model capable of qualitatively reproducing the asymmetric behavior is one capturing the combined motion of both skyrmions composing the ATM skyrmion. We start with the Thiele approximation for rigid skyrmions⁶,

$$G_i \hat{\mathbf{z}} \times (\mathbf{v}_e - \mathbf{v}_i) + \mathbf{D}_i (\beta \mathbf{v}_e - \alpha \mathbf{v}_i) + \mathbf{F} = 0, \quad (4)$$

where $\mathbf{D}_1 = \mathcal{D} \begin{pmatrix} 1 & \eta \\ \eta & \kappa \end{pmatrix}$ and $\mathbf{D}_2 = \mathcal{D} \begin{pmatrix} \kappa & \eta \\ \eta & 1 \end{pmatrix}$ are the dissipative tensors, G is the Magnus force strength, \mathbf{v}_e is the dragging force from STTs, \mathbf{v}_i is the velocity of each skyrmion component of the ATM skyrmion, α is the damping, the β term is responsible for nonadiabatic contributions from STTs, and \mathbf{F} is the net force from other interactions. We are using this model as a toy model, and therefore the values of these parameters do not directly correspond to those of our atomistic simulations. For a more accurate use of this equation, refer to Iwasaki *et al.*⁶. To account for the skyrmion asymmetry, we consider \mathbf{D} to have different components along each axis represented by the parameter κ . Assuming that the ATM skyrmion motion is given by $\mathbf{v} = (\mathbf{v}_1 + \mathbf{v}_2)/2$, using Eq. 4 and further assuming $\eta \ll 1$, $G_2 = -G_1 = G$, and taking $\mathbf{F} = 0$, we obtain

$$v_{\parallel} = \frac{v_e}{2} \frac{[\mathcal{D}G(\beta - \alpha)(\kappa - 1)\sin(2\phi) + 2\mathcal{D}^2\alpha\beta\kappa + 2G^2]}{\mathcal{D}^2\alpha^2\kappa + G^2} \quad (5)$$

$$v_{\perp} = \frac{v_e}{2} \frac{\mathcal{D}G(\beta - \alpha)(\kappa - 1)\cos(2\phi)}{\mathcal{D}^2\alpha^2\kappa + G^2}, \quad (6)$$

where v_{\parallel} and v_{\perp} are the velocities along and perpendicular to the applied current. We emphasize that this is a toy model and not a real model of the system.

In Fig. 4(a,b) we plot the Hall angle θ_{Hall} and the ATM skyrmion absolute velocity v , respectively, versus ϕ obtained using Eqs. 5, 6 with an arbitrary set of parameters. The Hall angle plot is very similar to the behavior observed in Figs. 2(a) and 3(a); however, the velocity curves differ from the velocities shown in Figs. 2(c) and 3(c). As previously stated, the

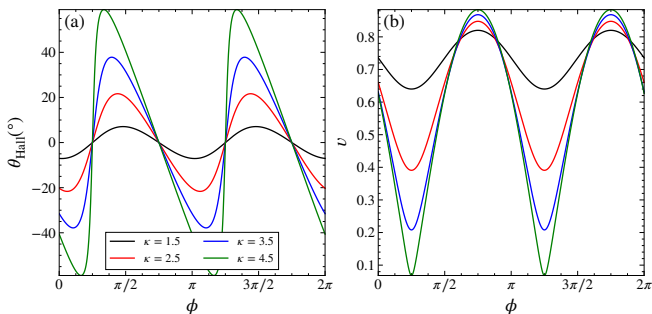


FIG. 4. Results of the ATM skyrmion behavior using the toy model from Eq. 4 with parameters $G = \mathcal{D} = v_e = 1$, $\alpha = 0.5$, $\beta = 0.01\alpha$ and different $\kappa = 1.5$ (black), 2.5 (red), 3.5 (blue), and 4.5 (green). (a) ATM skyrmion Hall angle θ_{Hall} vs applied current angle ϕ . (b) ATM skyrmion absolute velocity v vs applied current angle ϕ .

goal of our toy model is to reproduce the asymmetric behavior present in Figs. 2, 3. In Fig. 4(a), the current angles ϕ for which $\theta_{\text{Hall}} = 0$ match those found in Figs. 2(a) and 3(a). The sawtooth asymmetry is also captured by the toy model, especially for large values of κ . Since κ dictates how asymmetrical the ATM skyrmion is, large κ values correspond to large values of J_2/J_1 . The velocity curve of the toy model in Fig. 4(b) resembles the curves shown in Figs. 2(c) and 3(c), with $v \approx 0$ when $\phi = \pi/4 + n\pi$ and peak velocities at $\phi = 3\pi/4 + n\pi$; however, the limit of $\kappa \approx 1$ differs from the limit of $J_2/J_1 \approx 1$. Comparing these results, we can confidently say that the toy model correctly captures the most important behaviors of the ATM skyrmions, namely (i) the reduced velocity at $\phi = \pi/4 + n\pi$, (ii) the peak velocity at $\phi = 3\pi/4 + n\pi$, (iii) the fact that $\theta_{\text{Hall}} = 0$ when $\phi = \pi/4 + n\pi/2$, and (iv) the sawtooth shape of θ_{Hall} curve when the asymmetry of the ATM skyrmions is strong.

IV. EFFECTS OF PINNING

We next consider the effects of pinning on an ATM skyrmion. In Fig. 5(a), we show the energy profile as a function of relative position for an ATM skyrmion interacting with a circular pinning site of radius 1.5 nm, calculated using the atomistic model. Figure 5(b) shows the cross section ΔE of the energy for slices along $\theta = 0^\circ$, 32° , 60° , and 88° as a function of the distance r from the pinning site center. The peak in ΔE appears at a position just outside the entry of the skyrmion into the pinning site, and the dip to smaller energy for $r < 10$ nm indicates that the skyrmion core is pinned. Here, we can see that the anisotropic aspect of the pinning occurs due to the anisotropy of the ATM skyrmion itself; this effect is stronger for smaller r , whereas the behavior becomes more isotropic for larger r . This anisotropy means that the skyrmions become pinned most easily at different r values depending upon the relative direction between the skyrmion core and the pinning site center. For $r > 15$ nm, the pinning site appears more isotropic to the skyrmion. Due to the anisotropy of the pinning effectiveness, the depinning threshold for a trapped skyrmion

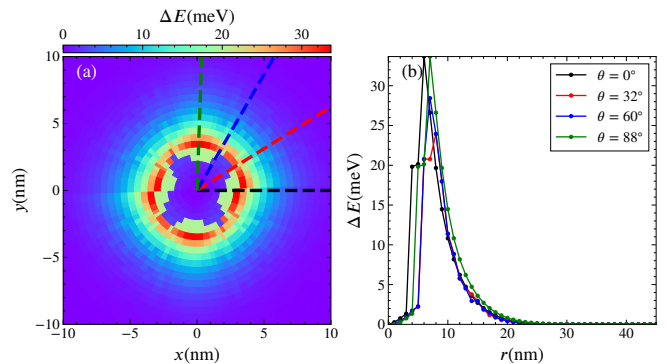


FIG. 5. (a) Atomistic simulation calculations of the interaction energy of ATM skyrmions as a function of y vs x position relative to the pinning site center for circular pinning sites with a radius of 1.5 nm. The maximum energy occurs just before the skyrmion becomes core pinned. For $r < 15$ nm, the pinning energy is anisotropic due to the anisotropic shape of the skyrmion. (b) Cross-sections of ΔE vs r for $\theta = 0.0^\circ$ (black), 32° (red), 60° (blue), and 88° (green) taken along the dashed lines in panel (a).

differs for different directions of the applied drive. In contrast, for ferromagnetic skyrmions, the pinning energy is isotropic, and the depinning threshold for different drive directions is also isotropic.

We next perform atomistic simulations for skyrmions interacting with a square array of high anisotropy pinning sites. Previous studies examined ferromagnetic skyrmions interacting with periodic defect arrays, and showed that the skyrmion Hall angle depends on the skyrmion velocity⁵⁹. This effect was also observed in simulations and experiments on random pinning arrays^{14,16,18–21} and arises due to a side-jump effect in which the Magnus force causes a preferential scattering off the pinning site. Slower skyrmions experience a larger jump, while fast-moving skyrmions are not as affected by the side jump and move more nearly along the intrinsic Hall angle of the pinning-free system^{12,59,60}.

In Fig. 6(a), we show the distance traveled by an ATM skyrmion, $\Delta r = \sqrt{\Delta x^2 + \Delta y^2}$, as a function of J_2/J_1 for skyrmions moving over a square defect array at a fixed current of $j = 5 \times 10^{10} \text{ Am}^{-2}$ and drive direction $\phi = 0^\circ$. At lower J_2/J_1 , the skyrmion motion is locked to 0° , even though there is a finite skyrmion Hall angle for these parameters in the absence of pinning. As J_2/J_1 increases, the skyrmion velocity in the pin-free case increases, as shown in Fig. 3(c). When pinning is present, however, the velocity decreases with increasing J_2/J_1 , which corresponds to a decrease in Δr in Fig. 6(a). For increasing J_2/J_1 , the skyrmion Hall angle for the pin-free system also increases, as seen in Fig. 3(a), but when pinning is present, the skyrmion moves only along the x -direction for $J_2/J_1 < 2.7$. We show this more clearly in Fig. 6(b), where we highlight ATM skyrmion trajectories for different J_2/J_1 values. The motion is locked in the x -direction for $J_2/J_1 \lesssim 2.7$, while for higher J_2/J_1 , the skyrmion travels at a 45° angle with respect to the pinning array. This means that just above $J_2/J_1 = 2.7$, the skyrmion Hall angle is larger than would be expected for the pin-free system. This is due to the locking

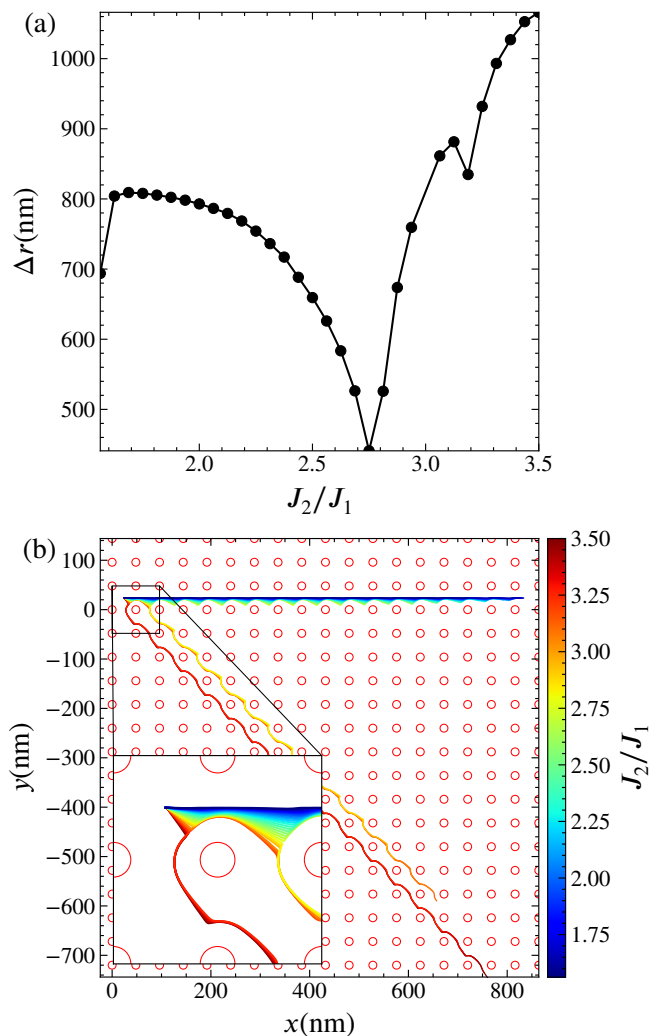


FIG. 6. Atomistic simulations of ATM skyrmions interacting with a square defect array with different J_2/J_1 at fixed $j = 5 \times 10^{10} \text{ A m}^{-2}$ and $\phi = 0$. (a) Net displacement $\Delta r = \sqrt{\Delta x^2 + \Delta y^2}$ vs J_2/J_1 . (b) ATM skyrmion trajectories as a function of y vs x at different J_2/J_1 values. The inset shows a detail of the splitting between the three observed flow directions.

of the skyrmion motion to a substrate symmetry direction. It is possible that for less dense pinning or smaller pinning sites, the motion would have locked to a smaller angle, such as one in which the skyrmion translates by three substrate lattice constants in x for every one lattice constant in y to give $\theta = 17.8^\circ = \arctan(1/3)$. The inset in Fig. 6(b) shows a detail of the skyrmion trajectories for increasing J_2/J_1 . The skyrmions attempt to move along the y -direction, but strike the next pinning site and are scattered back into motion along the x -direction. When J_2/J_1 and thus the skyrmion Hall angle is large enough, the skyrmions begin to travel along both the x and y directions because the skyrmion trajectory is bent strongly enough to pass by the pinning site without being scattered into the x direction. The transition point at which x and y motion first occurs corresponds to the J_2/J_1 value that produces a minimum in Δr . After the transition to motion along

45° , the skyrmion travels more rapidly with increasing J_2/J_1 , as indicated by the increase in Δr in Fig. 6(a) for $J_2/J_1 > 2.7$. A dip in Δr appears at $J_2/J_1 = 3.2$, corresponding to the point at which the initial skyrmion motion passes to the left rather than the right of the first pinning site in the inset of Fig. 6(b). In previous work on ferromagnetic skyrmions moving over a square periodic array, it was found that the skyrmion motion locks to symmetry directions such as 0° , 45° , and 90° , as well as other directions corresponding to $\theta = \arctan(n/m)$ with integer m and n . Here, the skyrmion travels by n pinning lattice sites in one direction and m pinning sites in the other direction, and the skyrmion velocity passes through a dip near these directional locking transitions.

We next consider an ATM skyrmion moving over a random array of pinning sites, which we simulate using our particle model. We turn to the particle model due to the computational cost of simulating atomistic ATM skyrmions. The reduction in the skyrmion velocity by the random pinning array means that it is necessary to go out to longer simulation times to observe the behavior, requiring substantially more computation compared to the periodic pinning array or the pin-free system. When considering the square-array we fixed j and ϕ while varying only J_2/J_1 ; however, in order to investigate the dynamics for random pinning, we must vary both j and ϕ while holding J_2/J_1 fixed, increasing the computational cost even further. Thus, only simulations with the particle model are practical. For the particle model, we consider a two-dimensional system of size 36×36 with periodic boundary conditions and $N_p = 100$ repulsive pinning sites with the Gaussian form $U(r) = U_0 \exp(-r^2/a_0^2)$, where $U_0 = 1.0$ and the pin radius $a_0 = 1.0$. We fix $G = \mathcal{D} = 1$, $\alpha = 0.5$, $\beta = 0.01\alpha$, and $\kappa = 4.5$ in Eq. 4. The driving force \mathbf{v}_e is $\mathbf{v}_e = v_e (\cos \phi \hat{\mathbf{x}} + \sin \phi \hat{\mathbf{y}})$.

In Fig. 7(a), we plot the velocity $\langle v \rangle$ versus the driving force v_e , which is associated with the velocity of the conduction electrons⁶, for different current directions ϕ . Both the depinning threshold and the velocity of the moving skyrmions change as ϕ is varied. Figure 7(b) shows the corresponding skyrmion Hall angle θ_{Hall} versus v_e for different ϕ . The variation of the skyrmion Hall angle with ϕ in the pin-free system was shown in Fig. 3(a) for the atomistic simulations and in Fig. 4(a) for the particle-based simulation. In the presence of random pinning, Fig. 7(b) indicates that the AFM skyrmion Hall angle changes very little with increasing v_e . For a ferromagnetic skyrmion, the skyrmion Hall angle is known to have a strong drive dependence when pinning is present, as has been shown in continuum¹⁹ and particle-based simulations^{14,61} and in experiments^{18,20,21}. In Fig. 8(a,b), we plot $\langle v \rangle$ and θ_{Hall} versus v_e from particle simulations of a ferromagnetic (FM) skyrmion at $\phi = 0^\circ, 30^\circ, 60^\circ, 75^\circ$ and 90° , using the same pinning parameters as in Fig. 7 for the ATM skyrmion. We note that these simulations are performed using the same equation as for the ATM skyrmion, Eq. 4, but since the different G skyrmions do not need to be “coupled,” these equations become effectively the same as those presented in Ref. 6. In Fig. 8(a), the depinning threshold for FM skyrmions is generally lower than that for ATM skyrmions, and the sliding velocity for v_e above the depinning threshold shows far

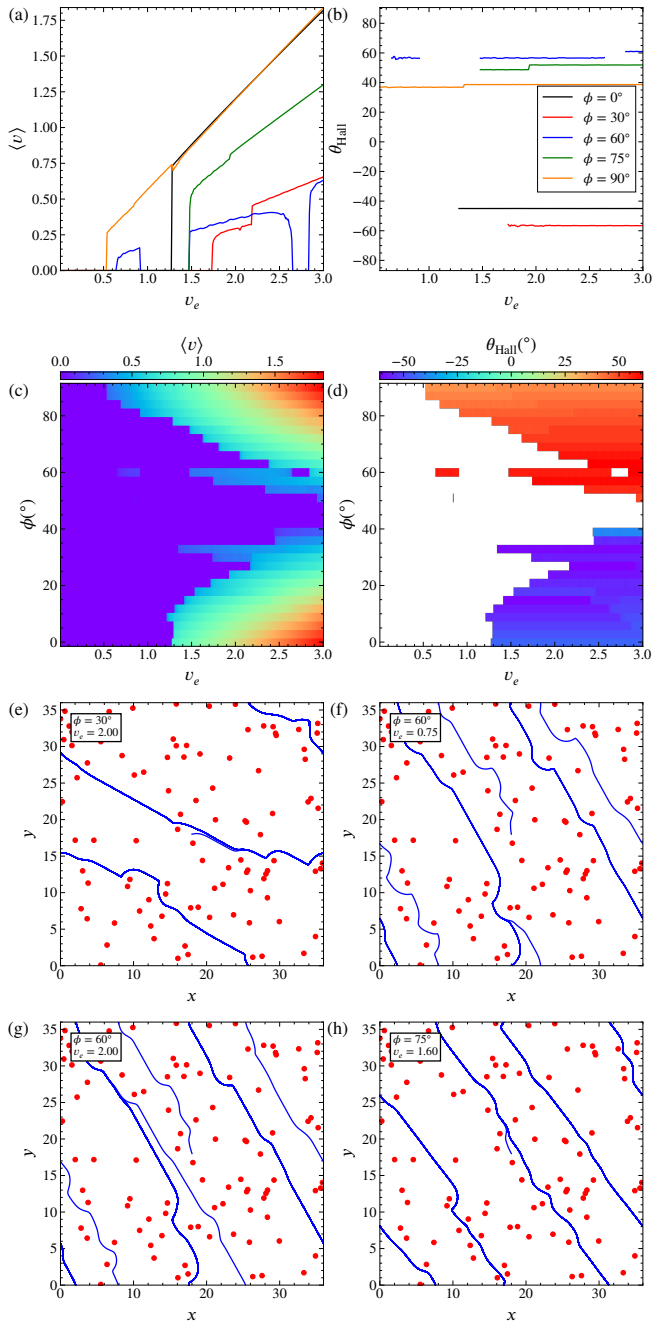


FIG. 7. Particle model simulations of ATM skyrmions interacting with a random array of repulsive pinning sites. (a) $\langle v \rangle$ vs drive v_e for drive directions $\phi = 0.0^\circ$ (black), 30° (red), 60° (blue), 75° (green), and 90° (orange). (b) The corresponding Hall angle θ_{Hall} vs v_e . (c) Heat map of $\langle v \rangle$ as a function of ϕ vs v_e . Here, the depinning threshold is anisotropic with a maximum near $\phi = 50^\circ$. (d) Heat map of θ_{Hall} as a function of ϕ vs v_e . There is almost no change in θ_{Hall} with varying v_e . (e-h) Skyrmion trajectories (lines) and pinning site locations (red dots) for the ATM skyrmions at (e) $\phi = 30^\circ$ and $v_e = 2.0$, (f) $\phi = 60^\circ$ and $v_e = 7.5$, (g) $\phi = 60^\circ$ and $v_e = 2.0$, and (h) $\phi = 75^\circ$ and $v_e = 1.6$.

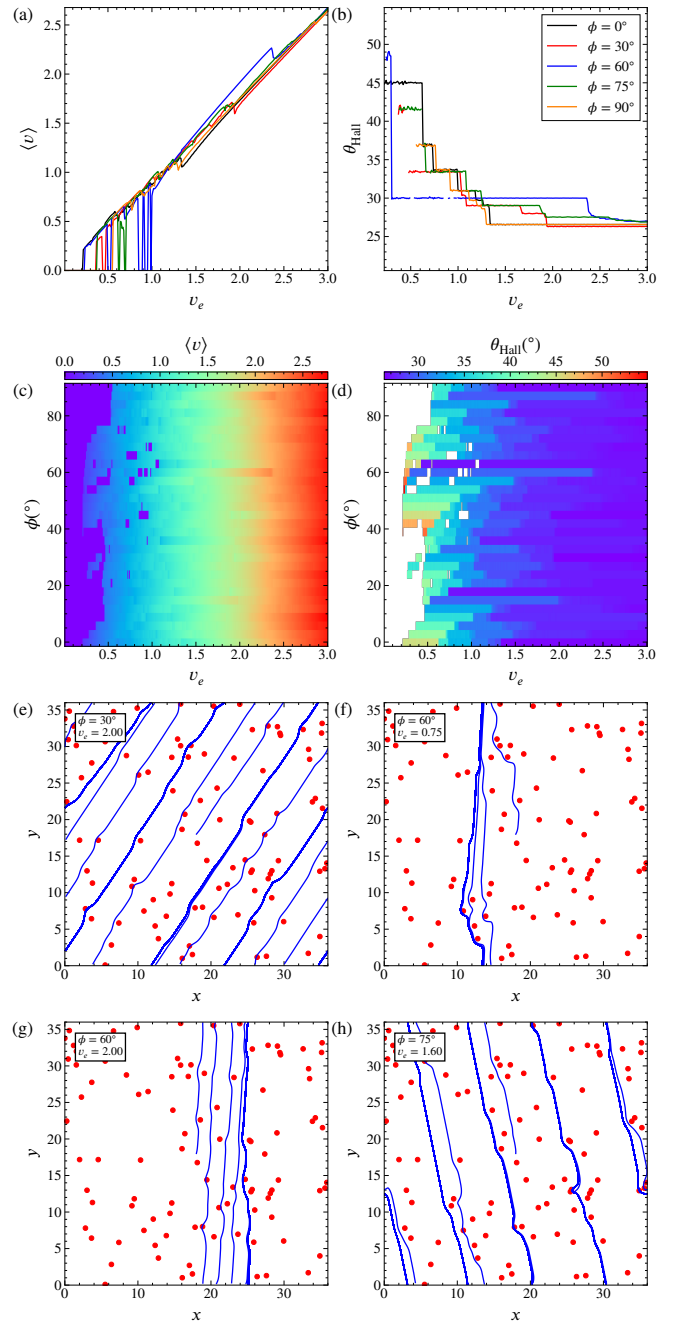


FIG. 8. Particle model simulations of FM skyrmions interacting with a random pinning array of repulsive pinning sites. (a) $\langle v \rangle$ vs v_e for $\phi = 0.0^\circ$ (black), 30° (red), 60° (blue), 75° (green), and 90° (orange). (b) The corresponding θ_{Hall} vs v_e . (c) Heat map of $\langle v \rangle$ as a function of ϕ vs v_e . Here, the depinning threshold is isotropic. (d) Heat map of θ_{Hall} as a function of ϕ vs v_e , showing a drive dependence of θ_{Hall} . (e-h) Skyrmion trajectories (lines) and pinning site locations (red dots) for the FM skyrmions at (e) $\phi = 30^\circ$ and $v_e = 2.0$, (f) $\phi = 60^\circ$ and $v_e = 7.5$, (g) $\phi = 60^\circ$ and $v_e = 2.0$, and (h) $\phi = 75^\circ$ and $v_e = 1.6$.

less variation than in the ATM skyrmion case. In Fig. 8(b), θ_{Hall} decreases with increasing v_e , in agreement with the expected velocity dependence of θ_{Hall} found in previous work on non-ATM skyrmions^{14,18–21}. When $\phi \geq 20^\circ$, θ_{Hall} approaches the intrinsic Hall value at higher v_e .

In Fig. 7(c), we plot a heat map of the skyrmion velocity $\langle v \rangle$ for the ATM skyrmions as a function of ϕ versus v_e , and in Fig. 7(d) we show the corresponding heat map of θ_{Hall} as a function of ϕ versus v_e . Here, the depinning threshold is anisotropic, with a maximum near $\theta = 45^\circ$ and a minimum at 0° and 90° . A similar anisotropy appears in the skyrmion velocities. In contrast, the heat maps of $\langle v \rangle$ and θ_{Hall} as a function of ϕ versus v_e shown in Fig. 8(c,d), respectively, for the FM skyrmions show that the depinning threshold is isotropic, with a low depinning threshold that is close to $v_e = 0.5$ regardless of the drive direction, and that the velocity response is also isotropic in the moving phase. For the ATM skyrmions in Fig. 7(d), θ_{Hall} is zero in the pinned region and is positive for $\phi > 45^\circ$ and negative for $\phi < 45^\circ$, reflecting the anisotropic nature of the ATM skyrmions. Additionally, in the moving phase, the Hall angle of the ATM skyrmions has little dependence on v_e in Fig. 7(d), whereas for FM skyrmions in Fig. 8(d), θ_{Hall} shows a clear drive dependence with increasing v_e , in agreement with previous work on FM skyrmions^{14,18–21}.

In Fig. 7(e,f,g,h), we image the ATM skyrmion trajectories for $\phi = 30^\circ$ and $v_e = 2.0$, $\phi = 60^\circ$ and $v_e = 0.75$, $\phi = 60^\circ$ and $v_e = 2.0$, $\phi = 75^\circ$ and $v_e = 1.6$, respectively. For $\phi = 30^\circ$ and $v_e = 2.0$ in Fig. 7(e), after an extremely brief transient, the skyrmion runs across the periodic boundary conditions and follows the same path during each set of passes across the system. In Fig. 7(f) at $\phi = 60^\circ$ and $v_e = 0.75$, the motion occurs at a larger angle to the driving direction, and the skyrmion trajectory has become more random and follows a different path during each traversal of the system. For $\phi = 60^\circ$ and $v_e = 2.0$ in Fig. 7(g), the trajectories are very similar to those shown at $v_e = 0.75$ in Fig. 7(f), reflecting the fact that there is little change in the Hall angle θ_{Hall} as a function of drive for the ATM skyrmions. In Fig. 7(h) at $\phi = 75^\circ$ and $v_e = 1.6$, the trajectories look similar to those found at $\phi = 30^\circ$ and $v_e = 2.0$, but the angle of travel is now larger.

The trajectories of the FM skyrmions appear in Fig. 8(e,f,g,h) at the same values of $\phi = 30^\circ$ and $v_e = 2.0$, $\phi = 60^\circ$ and $v_e = 0.75$, $\phi = 60^\circ$ and $v_e = 2.0$, and $\phi = 75^\circ$ and $v_e = 1.6$, respectively. For $\phi = 30^\circ$ and $v_e = 2.0$, Fig. 8(e) shows that the FM skyrmions travel more rapidly than the ATM skyrmions, and the motion is more random. The FM skyrmions also interact with the pinning sites differently, in that a moving skyrmion which approaches a pinning site very closely spirals around the pinning site due to the Magnus force. This spiraling motion of FM skyrmions around attractive or repulsive pinning sites has been studied in previous computational work and has been argued to be one of the reasons that FM skyrmions are weakly pinned compared to particles that do not have a Magnus force^{6,8,14,59,60,62}. When the Magnus force is small, the skyrmion moves parallel to the maximum direction of force, which points either directly toward or directly away from an attractive or repulsive pin, respectively. In Figs. 7 and 8, the pinning sites are repulsive,

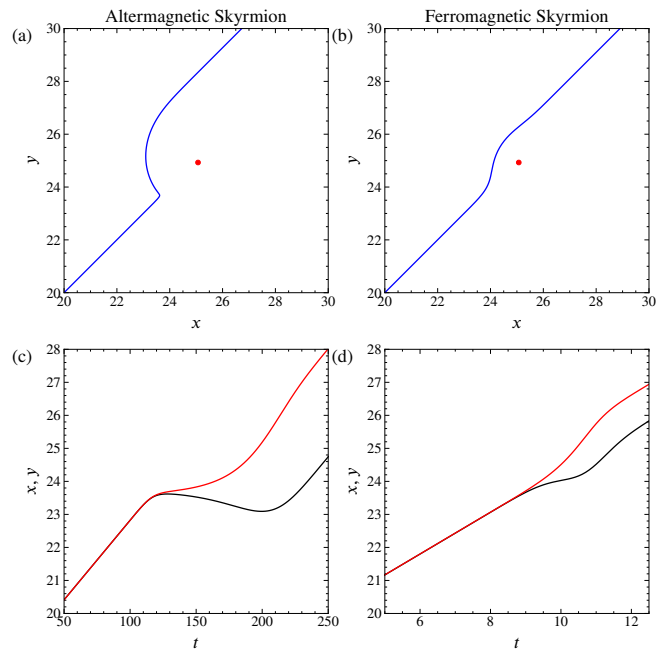


FIG. 9. (a) The position and trajectory of an ATM skyrmion interacting with a pinning site, where the skyrmion moves toward the pinning site with an impact parameter of 0.1. (b) The position and trajectory of a FM skyrmion under the same conditions. The FM skyrmion does not slow down as much and more easily moves around the pinning site. (c) The x (red) and y (black) positions of the ATM skyrmion from panel (a) vs time t . (d) The x (red) and y (black) positions of the FM skyrmion from panel (b) vs t .

and if the Magnus force is zero, as in the AFM skyrmions of Fig. 7, a skyrmion that moves toward a pinning site experiences a force in the direction opposite to the motion and will have difficulty moving around the pinning site. If there is a cluster of pinning sites present, the ATM skyrmion can be trapped. When the Magnus force is finite, as in the FM skyrmions of Fig. 8, there is an additional velocity component perpendicular to the force from the pinning, permitting the skyrmion to more easily move around the pinning site, and permitting even a cluster of pinning sites to be skirted. As the skyrmion moves around the pinning sites, it also experiences a side jump effect, and depending on the sign of the Magnus force, the side jump preferentially pushes the skyrmion to one side of the pinning sites, even when the impact factor would have caused the skyrmion to pass to the other side of the pinning site in the absence of a Magnus force. In Fig. 8(e,f,g,h), it is clear that the FM skyrmions preferentially move around the pinning sites to one side.

To show more clearly how the pinning is enhanced for an ATM skyrmion compared to a FM skyrmion, in Fig. 9(a) we plot the trajectory of a single ATM skyrmion moving toward a pinning site with an impact parameter of 0.1, which is just off-center. Figure 9(c) shows the corresponding x and y position of the skyrmion as a function of time. Upon approaching the pinning site, the ATM skyrmion slows down, and then undergoes a strong deviation to the side of the pinning site.

Throughout the motion, the minimum distance between the skyrmion and the pinning site remains relatively large. Figures 9(b) and (d) show the trajectory and time dependent positions, respectively, of a FM skyrmion under the same conditions, where we have chosen parameters such that the FM skyrmion approaches the pinning site at the same angle as the ATM skyrmion. We find that the FM skyrmion does not slow down as much as it nears the pinning site, and the minimum distance to the pinning site is much smaller than in the ATM case. The FM skyrmion also experiences less deviation as it moves past the pinning site compared to the ATM skyrmion. This indicates that the Magnus force reduces the effectiveness of the pinning for the FM skyrmion compared to the ATM skyrmion.

V. DISCUSSION

In this work we considered the motion of individual skyrmions, but an interesting direction for future exploration would be to use the atomistic and particle models to study the collective dynamics of ATM skyrmions. One open question is how to model the skyrmion-skyrmion interaction potential for the ATM particle model. In many-particle models with FM skyrmions, the skyrmions are considered to experience a short-range, isotropic repulsion such as a Bessel function^{13,14} or an exponential repulsion^{63,64}. In the absence of pinning, the FM skyrmions form a triangular lattice^{13,14}, while when pinning is present, the FM skyrmions can form a disordered or polycrystalline state⁶⁵. For ATM skyrmions, the skyrmion-skyrmion interactions should be anisotropic, and the degree of anisotropy would depend on the different exchange interactions of the two sublattices as well as on the distance between the skyrmions.

In Fig. 10, we show atomistic simulations of the trajectories of a pair of FM skyrmions and, separately, a pair of ATM skyrmions that are initially placed near each other. The FM skyrmions move in an outward spiral due to skyrmion-skyrmion repulsion combined with the Magnus force, while the ATM skyrmions, though clearly repelled by each other, move mostly outward due to the weaker Magnus force. A collective particle model for ATM skyrmions with the same isotropic Bessel function used for FM skyrmions could be a good approximation for low densities where the anisotropic part of the potential does not overlap. At higher densities, however, the skyrmion-skyrmion interactions would become more anisotropic, which could lead to the formation of a square lattice similar to that found in certain superconducting vortex systems with anisotropic interactions^{66,67}.

It is known that under a dc drive, FM skyrmions moving over quenched disorder can undergo dynamical transitions from a pinned glass to disordered plastic flow and a higher-drive triangular lattice, and that these transitions are independent of the direction of the dc drive¹⁴. For ATM skyrmions, the extent of the different dynamical phases could depend on the drive direction. There could be a stronger disordered flow regime for driving at 45° where the depinning threshold is higher, compared to driving along 0° or 90° .

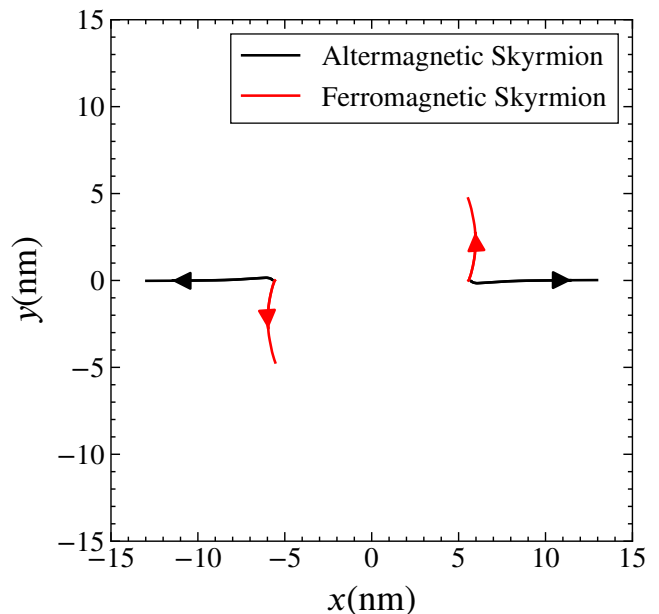


FIG. 10. Atomistic simulation of the trajectories of two FM skyrmions (red) and two ATM skyrmions (black) placed near each other. The FM skyrmions move outward with a spiraling motion due to the Magnus term, and there is skyrmion-skyrmion repulsion. The ATM skyrmions show strong repulsion but the spiraling component of the motion is greatly reduced.

Another question is the effect of thermal fluctuations on ATM skyrmions. At high enough temperatures, the system should undergo Brownian-like diffusion, similar to that found for FM skyrmions^{68–71}. In the presence of a rough landscape, the diffusion or thermal creep might be different between the two systems, however, and the diffusion might be anisotropic for ATM skyrmions but isotropic for FM skyrmions. Finally, there could be interesting features in the internal excitation modes of ATM versus FM skyrmions to examine in the atomistic and micromagnetic models. The low skyrmion Hall angle for ATM skyrmions is appealing for possible future applications, but the fact that ATM skyrmions are more susceptible to pinning compared to FM skyrmions could limit their usefulness.

VI. SUMMARY

Using atomistic simulations, we have studied the driven dynamics of skyrmions in an altermagnet (ATM). We find that the ATM skyrmion velocity and Hall angle are anisotropic, and that as the ratio of the exchange constants J_2/J_1 increases, the skyrmion becomes increasingly ellipsoidal in shape and shows increasing anisotropy in the Hall angle and velocity. We also propose a particle model for the AFM skyrmion that is simpler than the one presented by Jin *et al.*⁵⁰. In our model, we consider the dissipation components to vary with the sublattice directions. Despite the simplicity of the model, it captures the same general features as the atomistic model, includ-

ing the variation in the skyrmion Hall angle and velocity for changing drive direction. Using an atomistic model, we find that when an ATM skyrmion interacts with a pinning site, the pinning is anisotropic at shorter distances due to the shape of the skyrmion. For an ATM skyrmion interacting with a periodic array of pinning sites for a fixed drive direction, we find that as the ratio J_2/J_1 increases, the skyrmion motion transitions between symmetry directions from being locked along 0° to being locked along 45° , with a dip in velocity occurring at the transition. For an ATM skyrmion moving over random pinning, we find that the depinning threshold and velocity of the moving skyrmion are strongly anisotropic, and the skyrmion Hall angle shows little change with increasing drive. In contrast, for FM skyrmions, the depinning threshold is isotropic, and the skyrmion Hall angle has a strong drive dependence due to the presence of the Magnus force, which

creates a side jump effect. In general, ATM skyrmions are more strongly affected by pinning than FM skyrmions due to the reduction of the Magnus force. We also discuss several future directions, such as collective and thermal effects for ATM skyrmions.

ACKNOWLEDGMENTS

This work was supported by the US Department of Energy through the Los Alamos National Laboratory. Los Alamos National Laboratory is operated by Triad National Security, LLC, for the National Nuclear Security Administration of the U. S. Department of Energy (Contract No. 892333218NCA000001). We would like to thank Dr. Pablo Venegas for providing the computational resources used in this work via FAPESP (Grant: 2024/02941-1).

-
- * Corresponding author: jcsouza@dac.unicamp.br
- 1 S. Mühlbauer, B. Binz, F. Jonietz, C. Pfleiderer, A. Rosch, A. Neubauer, R. Georgii, and P. Böni, “Skyrmion lattice in a chiral magnet,” *Sci* **323**, 915–919 (2009).
 - 2 X. Z. Yu, Y. Onose, N. Kanazawa, J. H. Park, J. H. Han, Y. Matsui, N. Nagaosa, and Y. Tokura, “Real-space observation of a two-dimensional skyrmion crystal,” *Nature (London)* **465**, 901–904 (2010).
 - 3 S. Seki, X. Z. Yu, S. Ishiwata, and Y. Tokura, “Observation of skyrmions in a multiferroic material,” *Sci* **336**, 198–201 (2012).
 - 4 F. Jonietz, S. Mühlbauer, C. Pfleiderer, A. Neubauer, W. Münzer, A. Bauer, T. Adams, R. Georgii, P. Böni, R. A. Duine, K. Everschor, M. Garst, and A. Rosch, “Spin transfer torques in MnSi at ultralow current densities,” *Sci* **330**, 1648–1651 (2010).
 - 5 T. Schulz, R. Ritz, A. Bauer, M. Halder, M. Wagner, C. Franz, C. Pfleiderer, K. Everschor, M. Garst, and A. Rosch, “Emergent electrodynamic of skyrmions in a chiral magnet,” *Nat. Phys.* **8**, 301–304 (2012).
 - 6 J. Iwasaki, M. Mochizuki, and N. Nagaosa, “Universal current-velocity relation of skyrmion motion in chiral magnets,” *Nature Commun.* **4**, 1463 (2013).
 - 7 L. Kong and J. Zang, “Dynamics of an insulating skyrmion under a temperature gradient,” *Phys. Rev. Lett.* **111**, 67203 (2013).
 - 8 N. Nagaosa and Y. Tokura, “Topological properties and dynamics of magnetic skyrmions,” *Nat. Nanotechnol.* **8**, 899–911 (2013).
 - 9 M. Mochizuki, X. Z. Yu, S. Seki, N. Kanazawa, W. Koshibae, J. Zang, M. Mostovoy, Y. Tokura, and N. Nagaosa, “Thermally driven ratchet motion of a skyrmion microcrystal and topological magnon Hall effect,” *Nat. Mater.* **13**, 241–246 (2014).
 - 10 S. L. Zhang, W. W. Wang, D. M. Burn, H. Peng, H. Berger, A. Bauer, C. Pfleiderer, G. van der Laan, and T. Hesjedal, “Manipulation of skyrmion motion by magnetic field gradients,” *Nat. Commun.* **9**, 2115 (2018).
 - 11 K. Everschor-Sitte, J. Masell, R. M. Reeve, and M. Kläui, “Perspective: Magnetic skyrmions - Overview of recent progress in an active research field,” *J. Appl. Phys.* **124**, 240901 (2018).
 - 12 I. L. Fernandes, J. Bouaziz, S. Blügel, and S. Lounis, “Universality of defect-skyrmion interaction profiles,” *Nature Commun.* **9**, 4395 (2018).
 - 13 S.-Z. Lin, C. Reichhardt, C. D. Batista, and A. Saxena, “Particle model for skyrmions in metallic chiral magnets: Dynamics, pinning, and creep,” *Phys. Rev. B* **87**, 214419 (2013).
 - 14 C. Reichhardt, D. Ray, and C. J. Olson Reichhardt, “Collective transport properties of driven skyrmions with random disorder,” *Phys. Rev. Lett.* **114**, 217202 (2015).
 - 15 Se. Woo, K. Litzius, B. Krüger, M.-Y. Im, L. Caretta, K. Richter, M. Mann, A. Krone, R. M. Reeve, M. Weigand, P. Agrawal, I. Lemesch, M.-A. Mawass, P. Fischer, M. Kläui, and G. S. D. Beach, “Observation of room-temperature magnetic skyrmions and their current-driven dynamics in ultrathin metallic ferromagnets,” *Nat. Mater.* **15**, 501–506 (2016).
 - 16 R. Juge, S.-G. Je, D. de Souza Chaves, L. D. Buda-Prejbeanu, J. Peña Garcia, J. Nath, I. M. Miron, K. G. Rana, L. Aballe, M. Foerster, F. Genuzio, T. O. Menteş, A. Locatelli, F. Maccherozzi, S. S. Dhesi, M. Belméguenai, Y. Roussigné, S. Auffret, S. Pizzini, G. Gaudin, J. Vogel, and O. Boulle, “Current-driven skyrmion dynamics and drive-dependent skyrmion Hall effect in an ultrathin film,” *Phys. Rev. Applied* **12**, 044007 (2019).
 - 17 K. Everschor-Sitte and M. Sitte, “Real-space Berry phases: Skyrmion soccer (invited),” *J. Appl. Phys.* **115**, 172602 (2014).
 - 18 W. Jiang, X. Zhang, G. Yu, W. Zhang, X. Wang, M. B. Jungfleisch, J. E. Pearson, X. Cheng, O. Heinonen, K. L. Wang, Y. Zhou, A. Hoffmann, and S. G. E. te Velthuis, “Direct observation of the skyrmion Hall effect,” *Nat. Phys.* **13**, 162–169 (2017).
 - 19 W. Legrand, D. Maccariello, N. Reyren, K. Garcia, C. Moutafis, C. Moreau-Luchaire, S. Coffin, K. Bouzehouane, V. Cros, and A. Fert, “Room-temperature current-induced generation and motion of sub-100 nm skyrmions,” *Nano Lett.* **17**, 2703–2712 (2017).
 - 20 K. Litzius, I. Lemesch, B. Krüger, P. Bassirian, L. Caretta, K. Richter, F. Büttner, K. Sato, O. A. Tretiakov, J. Förster, R. M. Reeve, M. Weigand, I. Bykova, H. Stoll, G. Schütz, G. S. D. Beach, and M. Kläui, “Skyrmion Hall effect revealed by direct time-resolved X-ray microscopy,” *Nat. Phys.* **13**, 170–175 (2017).
 - 21 K. Zeissler, S. Finizio, C. Barton, A. J. Huxtable, J. Massey, J. Raabe, A. V. Sadovnikov, S. A. Nikitov, R. Brearton, T. Hesjedal, G. van der Laan, M. C. Rosamond, E. H. Linfield, G. Bunnell, and C. H. Marrows, “Diameter-independent skyrmion Hall angle observed in chiral magnetic multilayers,” *Nat. Commun.* **11**, 428 (2020).
 - 22 A. Fert, V. Cros, and J. Sampaio, “Skyrmions on the track,” *Nat. Nanotechnol.* **8**, 152–156 (2013).

- ²³ R. Tomasello, E. Martinez, R. Zivieri, L. Torres, M. Carpentieri, and G. Finocchio, “A strategy for the design of skyrmion race-track memories,” *Sci. Rep.* **4**, 6784 (2014).
- ²⁴ D. Pinna, G. Bourianoff, and K. Everschor-Sitte, “Reservoir computing with random skyrmion textures,” *Phys. Rev. Applied* **14**, 054020 (2020).
- ²⁵ K. M. Song, J.-S. Jeong, B. Pan, X. Zhang, J. Xia, S. Cha, T.-E. Park, K. Kim, S. Finizio, J. Raabe, J. Chang, Y. Zhou, W. Zhao, W. Kang, H. Ju, and S. Woo, “Skyrmion-based artificial synapses for neuromorphic computing,” *Nat. Electron.* **3**, 148–155 (2020).
- ²⁶ M. Hoffmann, B. Zimmermann, G. P. Müller, D. Schürhoff, N. S. Kiselev, C. Melcher, and S. Blügel, “Antiskyrmions stabilized at interfaces by anisotropic Dzyaloshinskii-Moriya interactions,” *Nature Commun.* **8**, 308 (2017).
- ²⁷ A. K. Nayak, V. Kumar, T. Ma, P. Werner, E. Pippel, R. Sahoo, F. Damay, U. K. Roessler, C. Felser, and S. S. P. Parkin, “Magnetic antiskyrmions above room temperature in tetragonal Heusler materials,” *Nature (London)* **548**, 561–566 (2017).
- ²⁸ H. Yoshimochi, R. Takagi, J. Ju, N. D. Khanh, H. Saito, H. Sagayama, H. Nakao, S. Itoh, Y. Tokura, T. Arima, S. Hayami, T. Nakajima, and S. Seki, “Multistep topological transitions among meron and skyrmion crystals in a centrosymmetric magnet,” *Nature Phys.* **20**, 1001–1008 (2024).
- ²⁹ J. Barker and O. A. Tretiakov, “Static and dynamical properties of antiferromagnetic skyrmions in the presence of applied current and temperature,” *Phys. Rev. Lett.* **116**, 147203 (2016).
- ³⁰ W. Legrand, D. Maccariello, F. Ajejas, S. Collin, A. Vecchiola, K. Bouzehouane, N. Reyren, V. Cros, and A. Fert, “Room-temperature stabilization of antiferromagnetic skyrmions in synthetic antiferromagnets,” *Nat. Mater.* **19**, 34–42 (2020).
- ³¹ V. T. Pham, N. Sisodia, I. Di Manici, J. Urrestarazu-Larrañaga, K. Bairagi, J. Pelloux-Prayer, R. Guedas, L. D. Buda-Prejbeanu, S. Auffret, A. Locatelli, T. O. Menteş, S. Pizzini, P. Kumar, A. Finco, V. Jacques, G. Gaudin, and O. Boulle, “Fast current-induced skyrmion motion in synthetic antiferromagnets,” *Science* **384**, 307–312 (2024).
- ³² A. G. Kolesnikov, M. E. Stebliy, A. S. Samardak, and A. V. Ognev, “Skyrmionium - high velocity without the skyrmion Hall effect,” *Sci. Rep.* **8**, 16966 (2018).
- ³³ Y. Liu, W. Hou, X. Han, and J. Zang, “Three-dimensional dynamics of a magnetic hopfion driven by spin transfer torque,” *Phys. Rev. Lett.* **124**, 127204 (2020).
- ³⁴ F. Zheng, N. S. Kiselev, F. N. Rybakov, L. Yang, W. Shi, S. Blügel, and R. E. Dunin-Borkowski, “Hopfion rings in a cubic chiral magnet,” *Nature (London)* **623**, 718–723 (2023).
- ³⁵ J. C. Bellizotti Souza, C. J. O. Reichhardt, C. Reichhardt, A. Saxena, N. P. Vizarim, and P. A. Venegas, “Topological transitions, pinning and ratchets for driven magnetic hopfions in nanostructures,” *Sci. Rep.* **15** (2025), 10.1038/s41598-025-01349-9.
- ³⁶ B. Göbel, I. Mertig, and O. A. Tretiakov, “Beyond skyrmions: Review and perspectives of alternative magnetic quasiparticles,” *Phys. Rep.* **895**, 1 (2021).
- ³⁷ J. C. Bellizotti Souza, N. P. Vizarim, C. J. O. Reichhardt, C. Reichhardt, and P. A. Venegas, “Comparing dynamics, pinning and ratchet effects for skyrmionium, skyrmions, and antiskyrmions,” *J. Phys.: Condens. Matter* **37**, 165801 (2025).
- ³⁸ A. Aldarawsheh, M. Sallermann, M. Abusaa, and S. Lounis, “Current-driven dynamics of antiferromagnetic skyrmions: from skyrmion hall effects to hybrid inter-skyrmion scattering,” *npj Spintronics* **2** (2024), 10.1038/s44306-024-00049-w.
- ³⁹ S. Wang, L. Yao, Y. Zhou, and S. Jiang, “Dynamical synthetic antiferromagnetic skyrmions and skyrmionia,” *Phys. Rev. Appl.* **24**, 034054 (2025).
- ⁴⁰ T. Dohi, S. DuttaGupta, S. Fukami, and H. Ohno, “Formation and current-induced motion of synthetic antiferromagnetic skyrmion bubbles,” *Nat. Commun.* **10** (2019), 10.1038/s41467-019-13182-6.
- ⁴¹ V. Baltz, A. Manchon, M. Tsoi, T. Moriyama, T. Ono, and Y. Tserkovnyak, “Antiferromagnetic spintronics,” *Rev. Mod. Phys.* **90**, 015005 (2018).
- ⁴² L. Šmejkal, J. Sinova, and T. Jungwirth, “Beyond conventional ferromagnetism and antiferromagnetism: A phase with nonrelativistic spin and crystal rotation symmetry,” *Phys. Rev. X* **12**, 031042 (2022).
- ⁴³ L. Šmejkal, J. Sinova, and T. Jungwirth, “Emerging research landscape of altermagnetism,” *Phys. Rev. X* **12**, 040501 (2022).
- ⁴⁴ L. Šmejkal, A. Marmodoro, K.-H. Ahn, R. González-Hernández, I. Turek, S. Mankovsky, H. Ebert, S. W. D’Souza, O. Šipr, J. Sinova, and T. Jungwirth, “Chiral magnons in altermagnetic ruO_2 ,” *Phys. Rev. Lett.* **131**, 256703 (2023).
- ⁴⁵ P. A. McClarty and J. G. Rau, “Landau theory of altermagnetism,” *Phys. Rev. Lett.* **132**, 176702 (2024).
- ⁴⁶ T. Jungwirth, J. Sinova, R. M. Fernandes, Q. Liu, H. Watanabe, S. Murakami, S. Nakatsuji, and L. Šmejkal, “Symmetry, microscopy and spectroscopy signatures of altermagnetism,” *Nature (London)* **649**, 837–847 (2026).
- ⁴⁷ S. Lee, S. Lee, S. Jung, J. Jung, D. Kim, Y. Lee, B. Seok, J. Kim, B. G. Park, L. Šmejkal, C.-J. Kang, and C. Kim, “Broken kramers degeneracy in altermagnetic mnt,” *Physical Review Letters* **132**, 036702 (2024).
- ⁴⁸ J. Krempaský, L. Šmejkal, S. W. D’Souza, M. Hajlaoui, G. Springholz, K. Uhlířová, F. Alarab, P. C. Constantinou, V. Strocov, D. Usanov, W. R. Pudelko, R. González-Hernández, A. Birk Hellenes, Z. Jansa, H. Reichlová, Z. Šobáň, R. D. Gonzalez Betancourt, P. Wadley, J. Sinova, D. Kriegner, J. Minár, J. H. Dil, and T. Jungwirth, “Altermagnetic lifting of Kramers spin degeneracy,” *Nature (London)* **626**, 517–522 (2024).
- ⁴⁹ F. Zhang, X. Cheng, Z. Yin, C. Liu, L. Deng, Y. Qiao, Z. Shi, S. Zhang, J. Lin, Z. Liu, M. Ye, Y. Huang, X. Meng, C. Zhang, T. Okuda, K. Shimada, S. Cui, Y. Zhao, G.-H. Cao, S. Qiao, J. Liu, and C. Chen, “Crystal-symmetry-paired spin–valley locking in a layered room-temperature metallic altermagnet candidate,” *Nat. Phys.* **21**, 760–767 (2025).
- ⁵⁰ Z. Jin, Z. Zeng, Y. Cao, and P. Yan, “Skyrmion hall effect in altermagnets,” *Phys. Rev. Lett.* **133**, 196701 (2024).
- ⁵¹ H. Vakili, E. Schwartz, and A. A. Kovalev, “Spin-transfer torque in altermagnets with magnetic textures,” *Phys. Rev. Lett.* **134**, 176401 (2025).
- ⁵² E. Schwartz, H. Vakili, and A. A. Kovalev, “Theory of thermomagnonic torques in altermagnets,” (2025), arXiv:2512.14660 [cond-mat.mes-hall].
- ⁵³ Y. Jiang, X. Chen, C. Xuan, Z. Wang, and H. Yu, “Altermagnet skyrmions: Macroscopic realization of d -wave symmetry,” *Phys. Rev. B* **112**, 014423 (2025).
- ⁵⁴ Y. Liu, Z. Jin, J. Liu, and P. Yan, “Current-driven nonlinear skyrmion dynamics in altermagnets,” (2026), arXiv:2601.13499 [cond-mat.mtrl-sci].
- ⁵⁵ S. Seki and M. Mochizuki, *Skyrmions in Magnetic Materials* (Springer International Publishing, Switzerland, 2016).
- ⁵⁶ T. L. Gilbert, “A phenomenological theory of damping in ferromagnetic materials,” *IEEE Trans. Mag.* **40**, 3443–3449 (2004).
- ⁵⁷ J. C. Slonczewski, “Dynamics of magnetic domain walls,” *AIP Conf. Proc.* **5**, 170–174 (1972).
- ⁵⁸ J. Zang, M. Mostovoy, J. H. Han, and N. Nagaosa, “Dynamics of skyrmion crystals in metallic thin films,” *Phys. Rev. Lett.* **107**, 136804 (2011).

- ⁵⁹ C. Reichhardt, D. Ray, and C. J. Olson Reichhardt, “Quantized transport for a skyrmion moving on a two-dimensional periodic substrate,” *Phys. Rev. B* **91**, 104426 (2015).
- ⁶⁰ J. Müller and A. Rosch, “Capturing of a magnetic skyrmion with a hole,” *Phys. Rev. B* **91**, 054410 (2015).
- ⁶¹ C. Reichhardt and C. J. O. Reichhardt, “Thermal creep and the skyrmion Hall angle in driven skyrmion crystals,” *J. Phys.: Condens. Matter* **31**, 07LT01 (2019).
- ⁶² I. L. Fernandes, J. Chico, and S. Lounis, “Impurity-dependent gyrotropic motion, deflection and pinning of current-driven ultrasmall skyrmions in PdFe/Ir(111) surface,” *Journal of Physics: Condensed Matter* **32**, 425802 (2020).
- ⁶³ Y. Wang, J. Wang, T. Kitamura, H. Hirakata, and T. Shimada, “Exponential temperature effects on skyrmion-skyrmion interaction,” *Phys. Rev. Appl.* **18**, 044024 (2022).
- ⁶⁴ Y. Ge, J. Rothörl, M. A. Brems, N. Kerber, R. Gruber, T. Dohi, M. Kläui, and P. Virnau, “Constructing coarse-grained skyrmion potentials from experimental data with Iterative Boltzmann Inversion,” *Commun. Phys.* **6** (2023), 10.1038/s42005-023-01145-9.
- ⁶⁵ R. Gruber, S. M. Fröhlich, J. Rothörl, M. A. Brems, T. Sparmann, F. Kammerbauer, M.-A. Syskaki, E. M. Jefremovas, S. Krishnia, A. Sudbø, P. Virnau, and M. Kläui, “Skyrmion lattice domain formation in a non-flat energy landscape,” *Commun. Phys.* **9** (2026), 10.1038/s42005-025-02462-x.
- ⁶⁶ R. Gilardi, J. Mesot, A. Drew, U. Divakar, S. L. Lee, E. M. Forgan, O. Zaharko, K. Conder, V. K. Aswal, C. D. Dewhurst, R. Cubitt, N. Momono, and M. Oda, “Direct evidence for an intrinsic square vortex lattice in the overdoped high- T_c superconductor $\text{La}_{1.83}\text{Sr}_{0.17}\text{CuO}_{4+\delta}$,” *Phys. Rev. Lett.* **88**, 217003 (2002).
- ⁶⁷ Y. Xie, N. Chalus, Z. Wang, W. Yao, J. Liu, Y. Yao, J. S. White, L. M. DeBeer-Schmitt, J.-X. Yin, P. Dai, and M. R. Eskildsen, “Conventional superconductivity in the doped kagome superconductor $\text{Cs}(\text{V}_{0.86}\text{Ta}_{0.14})_3\text{Sb}_5$ from vortex lattice studies,” *Nat. Commun.* **15** (2024), 10.1038/s41467-024-50856-2.
- ⁶⁸ L. Zhao, Z. Wang, X. Zhang, X. Liang, Xia J, K. Wu, H.-A. Zhou, Y. Dong, G. Yu, K. L. Wang, Liu X, Y. Zhou, and W. Jiang, “Topology-dependent Brownian gyromotion of a single skyrmion,” *Phys. Rev. Lett.* **125**, 27206 (2020).
- ⁶⁹ T. Dohi, M. Weißenhofer, N. Kerber, F. Kammerbauer, Y. Ge, K. Raab, J. Zázvorka, M.-A. Syskaki, A. Shahee, M. Ruhwedel, T. Böttcher, P. Pirro, G. Jakob, U. Nowak, and M. Kläui, “Enhanced thermally-activated skyrmion diffusion with tunable effective gyrotropic force,” *Nat. Commun.* **14** (2023), 10.1038/s41467-023-40720-0.
- ⁷⁰ P. Rieger, M. Weißenhofer, and U. Nowak, “Defect-enhanced diffusion of magnetic skyrmions,” *Phys. Rev. B* **108**, 144417 (2023).
- ⁷¹ X. Zhang, J. Xia, O. A. Tretiakov, M. Ezawa, G. Zhao, Y. Zhou, X. Liu, and M. Mochizuki, “Chiral skyrmions interacting with chiral flowers,” *Nano Lett.* **23**, 11793–11801 (2023).